

# Rotating Magnetic Miniature Swimming Robots With Multiple Flexible Flagella

Zhou Ye, *Student Member, IEEE*, Stéphane Régnier, and Metin Sitti, *Senior Member, IEEE*

**Abstract**—Recent studies have been carried out for rotating single flexible flagellum: a possible propelling mechanism that has been adopted by several artificial microswimmers due to its relatively simple structure yet considerable propulsive force generation. In this paper, we introduce a miniature swimming robot design with multiple flexible artificial flagella that benefits from the increased number of flagella. The characteristic length of the robot body is less than 1 mm. Experimental characterization of swimming of the robot shows that swimming speed can be linearly improved solely by increasing the number of attached flagella, suggesting a new way for speed enhancement besides flagellum geometry optimization. In addition, a numerical model modified from the single, straight flexible flagellum case is further established to study propulsive force generation by nonstraight, flexible flagellum. A robot with multiple, sinusoidal flagella design is fabricated to demonstrate the capability of the proposed two-step photolithography-based microfabrication method to handle more complex flagella designs, which may enhance swimming performance.

**Index Terms**—Magnetic actuation, microrobotics, multiple artificial flagella, swimming robot.

## I. INTRODUCTION

THREE-DIMENSIONAL (3-D) swimming locomotion of miniature robots has been an ongoing interest for many researchers due to its potential biomedical and microfluidic applications such as targeted drug delivery, microsurgery, and micromanipulation [1]–[5]. One of the major challenges for these mobile miniature robots is miniaturization limitation on on-board power sources and actuators [6]. Magnetic actuation using external electromagnetic coils or permanent magnets has been used as one of the promising solutions to such a challenge by remotely actuating miniature robots for various applications [7]–[16]. A weak magnetic field up to tens of mT is sufficient to actuate most of these magnetic microrobot designs, which makes it easy and safe to generate toward medical

Manuscript received July 26, 2013; revised; accepted August 24, 2013. This paper was recommended for publication by Associate Editor Y. Sun and Editor B. J. Nelson upon evaluation of the reviewers' comments. This work was supported in part by the program "Research in Paris."

Z. Ye and M. Sitti are with the Department of Mechanical Engineering, Carnegie Mellon University, Pittsburgh, PA 15213 USA (e-mail: zhouye@andrew.cmu.edu; sitti@cmu.edu).

S. Régnier is with the Institut des Systèmes Intelligents et de Robotique, Université Pierre et Marie Curie, Paris Cedex 75252, France (e-mail: stephane.regnier@upmc.fr).

This paper has supplementary downloadable material available at <http://ieeexplore.ieee.org>.

Color versions of one or more of the figures in this paper are available online at <http://ieeexplore.ieee.org>.

Digital Object Identifier 10.1109/TRO.2013.2280058

applications inside human body [17]. Besides magnetic actuation, several other powering methods have also been explored, including actuation by chemical reactions [18], [19] and living microorganisms [20]–[23]. However, magnetic actuation has a significant advantage comparing with these methods, which is that the motions of magnetically actuated robots are much more controllable than the ones actuated by other mechanisms.

Three-dimensional locomotion of magnetically actuated miniature robots in liquids is achieved using mainly two approaches. First, magnetic miniature robots are directly pulled by magnetic forces exerted by external magnetic field gradients, and thus, the robot's motion is purely translational. This mechanism is simple and straightforward, but the maximum force that can be exerted onto the robot and the resulting maximum velocity that the robot can achieve decreases drastically as the size of the robot decreases [24]. The second approach is based on small-scale propulsion mechanisms inspired by microorganisms, which are significantly different from those at the macroscale due to the dominant viscous forces at low Reynolds number (Re). Various small-scale propulsion mechanisms have evolved for microorganisms to confront this problem, among which two major mechanisms have been widely duplicated on many artificial miniature swimmers. For the first mechanism, thrust is generated by rotation of rigid helical flagella [25]. Zhang *et al.* [26] developed a 38- $\mu\text{m}$ -long rigid helical artificial flagellum which swam at the maximum speed of  $v_{\text{max}} = 18 \mu\text{m/s}$ , while Ghosh and Fischer [27] fabricated a similar helical swimmer that was more than ten times smaller in size (2  $\mu\text{m}$  in length) with improved swimming performance ( $v_{\text{max}} = 40 \mu\text{m/s}$ ). For the second mechanism, propulsion is realized by propagation of periodic traveling waves, either planar or 3-D, along the long flexible flagella [25]. Dreyfus *et al.* [28] first reported a 24- $\mu\text{m}$ -long flexible swimmer propelling by propagating a plane wave through its long tail consisting of colloidal magnetic particles. Cheang *et al.* [29] later reported a microswimmer that propelled itself by rotating a thin flexible flagellar filament (5.8  $\mu\text{m}$  long) attached to a 150-nm magnetic nanoparticle at one end and a 3- $\mu\text{m}$  polystyrene microbead at the other. Gao *et al.* [30] fabricated a rotation-based flexible nanowire motor that had three metal sections and a length of 6.5  $\mu\text{m}$ , which swam at  $v_{\text{max}} = 6 \mu\text{m/s}$ , while Pak *et al.* [31] improved the swimming performance ( $v_{\text{max}} = 21 \mu\text{m/s}$ ) by a new design that was 5.8  $\mu\text{m}$  in length and theoretically characterized the mechanism by an asymptotic analysis.

It is studied that in theory, using either a rigid helical artificial flagellum or a flexible artificial flagellum would lead to similar peak swimming velocities and energy efficiency assuming the same cross section and length and the same maximum

driving torque [24], [32]. On one hand, the advantage of using a rigid helical flagellum is that the propulsive force generated, the driving torque required, and the resulting swimming speed are linearly related to the driving rotation frequency [24]. In addition, the swimming direction can be reversed simply by switching the rotation direction [26]. Therefore, the control of swimming is relatively simple. On the other hand, one significant advantage of using a flexible flagellum design is that the flexibility of nonrigid flagella brings compliance to the swimmer, which would be desired for many biomedical applications for improved safety, especially when operating inside the human body [33]. Moreover, the structural simplicity of straight flexible artificial flagella could make fabrication simpler and less expensive as well.

All of the microscale swimming robots mentioned previously have only one artificial flagellum on each. At a larger scale of several millimeters, Garstecki *et al.* [34] reported a swimmer that had two flexible wings using a similar mechanism of rotating these wings to propel itself at low and medium  $Re$ . Experiments on mesoscale fixed-end artificial flagella have demonstrated that an increase in the number of flexible flagella under some conditions leads to extra propulsion [35]. However, real miniature swimming robots taking full advantage of multiple artificial flexible flagella have yet to be developed.

In this study, we introduce a submillimeter-scale swimming robot design that equips with flexible straight flagella, which could improve swimming speeds almost linearly with the number of attached flagella of up to four. The numerical simulation results based on single-flexible-flagellum models derived from previous works [31], [36]–[41] with modified boundary conditions provide the guideline for our flagella design. Optimization is then performed to examine the influence of each design parameter on the generated propulsive force and to search for an optimized flagellum design, which produces a large propulsive force per unit length of robot. A numerical model modified from the straight flagellum case is further established to preliminarily examine the effect of flagellum’s intrinsic curvature on the propulsive force generated. We apply this model on a flagellum with planar sinusoidal shape, the result of which indicates that flagellum curvature could increase propulsive force. All the flagellated robots are fabricated via a simple, inexpensive, yet repeatable method, which includes two steps of micromolding with a manual assembly step to combine two-dimensional (2-D) structures into a 3-D structure, inspired by [42]. Besides the simple straight flagella design, we demonstrate that the proposed fabrication method has the capability to fabricate flagella with more complex planar geometries, for instance, sinusoidal curves. Experimental characterization is carried out for the translational speeds of swimming robots with different numbers of flagella under different rotation frequencies at low  $Re$  ( $Re \ll 1$ ), which shows that swimming performance could be improved by increasing the number of flagella. The propulsion mechanism is also demonstrated to work in a large range of viscosities.

While the numerical simulations in this study are based on models regardless of actual robot and flagella dimensions, the experimental results are derived from mesoscale swimming

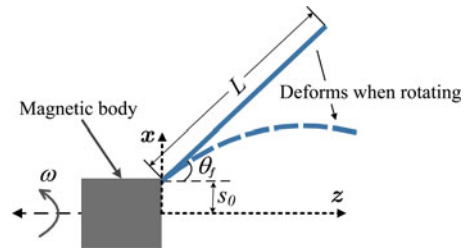


Fig. 1. Schematic of a magnetic single-flagellum swimming robot. The dark square represents the magnetic cylindrical body, while the solid blue line shows the undeformed, nonmagnetic artificial flagellum. When the robot body rotates, it conveys the rotation to the flexible flagellum, which then passively bends into chiral shape, as shown by the curved dotted blue line.

robot prototypes, which may not be suitable for some of the proposed potential applications, especially those inside human body, due to the relatively up-scaled size. However, these experimental results are expected to be applicable for micrometer-scale robots as well, considering that the  $Re$  of the motions of the proposed robots in highly viscous fluid is similar to that of micrometer-scale robots in fluids with low viscosity such as water and human blood plasma.  $Re$ , which is the ratio between inertial forces and viscous forces, can be used to determine hydrodynamic similarity between different flows. In the nondimensional form of the Navier–Stokes equations for incompressible flows,  $Re$  is the only parameter to measure the relative magnitude of terms in the equations [43]. Therefore, as long as the  $Re$  of two geometrically similar systems at different scales are the same, the flow patterns would be identical. Researchers have taken advantage of such hydrodynamic similarity between flows at different scales with similar  $Re$ . For example, scaled-up experimental setups have been well exploited to study hydrodynamics for micrometer-scale single-flagellum propulsion and proven to be valid [37], [39], [40]. In addition, mesoscale experiments have also been adopted to study hydrodynamic interactions at low  $Re$ , and good agreement with theoretical modeling was found [44], [45]. Considering that the hydrodynamic interactions are direct results from flow patterns, they are directly scalable between different flows with similar  $Re$ . Therefore, the modeling and experimental results from our mesoscale prototypes also provide design and actuation guidelines and swimming models for micrometer-scale swimmers.

## II. MODELING AND DESIGN

The magnetic miniature swimming robot consists of a cylindrical body made of a permanent-magnet-based composite (Neodymium–Iron–Boron (NdFeB) and polyurethane), which rotates under an applied rotating magnetic field. Flexible polymer flagella with length  $L$  are attached to the end of the body with an anchoring angle  $\theta_f$  and an offset  $s_0$  with respect to the body’s long axis, as shown in Fig. 1. When the robot body rotates about its long axis, the rotation is conveyed to the attached flagella. The originally straight, tilted, and offset flagella are then bent into chiral shapes in fluids by viscous drag, which results in a net axial force to propel the robot body in fluid.

The hydrodynamic models introduced in the following sections are established for the regime where  $Re \ll 1$ , regardless of the actual size of the structures, and, hence, are applicable to swimming robots not only at the scale of the current prototypes but at micrometer scales, as long as  $Re \ll 1$ .

### A. Magnetic Actuation

A magnetic miniature swimming robot body is rotated along its body axis by an applied rotating magnetic field. Similar magnetic control techniques have been reported in the literature [46]–[48] and are applicable to swimming robots made of not only hard but of soft magnetic materials as well. The magnetic torque applied on the robot body is given by

$$\mathbf{T}_m = V_m \mathbf{M} \times \mathbf{B} \quad (1)$$

where  $V_m$  and  $\mathbf{M}$  are the volume and magnetization of the robot body, respectively, and  $\mathbf{B}$  is the applied field. Considering the composite robot body made of magnetic NdFeB particles and polyurethane, its magnetization would be different from a solid magnetic material. As the mass ratio of NdFeB particles and polymer in the mixture,  $\alpha_m$ , can be adjusted during fabrication process, the magnetization can be determined as

$$\mathbf{M} = \frac{M_{\text{NdFeB}}}{1 + \rho_{\text{NdFeB}} / (\alpha_m \rho_{\text{poly}})} \quad (2)$$

where  $\rho_{\text{NdFeB}}$  and  $\rho_{\text{poly}}$  are the densities of NdFeB and polyurethane, respectively, and  $M_{\text{NdFeB}}$  is the magnetization of a solid NdFeB material. Therefore, the maximum magnetic torque that can be applied on a cylindrical robot body is

$$|\mathbf{T}_{\text{max}}| = V_m |\mathbf{M}| |\mathbf{B}| \sin \frac{\pi}{2} = \frac{\pi}{4} \frac{D^2 H |M_{\text{NdFeB}}| |\mathbf{B}|}{1 + \rho_{\text{NdFeB}} / (\alpha_m \rho_{\text{poly}})}. \quad (3)$$

Considering that the planar parts are made of nonmagnetic materials in the first step of fabrication, the effective volume  $V_e$  of NdFeB in the final robot body would be less than the total body volume  $V_m$ , i.e., typically about 60–80% of  $V_m$ , depending on the geometry of the planar part cross sections.

### B. Fluidic Drag Force and Torque on Robot Body

The robot body is modeled as a cylinder with a cross-sectional diameter  $D$  and a height  $H$ , and the aspect ratio ( $H/D$ ) is larger than 1. During swimming, the robot body undergoes two simultaneous motions: rotation around its body axis and translation along the same axis. Due to low  $Re$ , these two motions can be decoupled and analyzed separately, and the complete motion is the linear superposition of the two. The resistive fluidic drag force due to the translational motion of the cylindrical body is approximated by [49]

$$\begin{aligned} \mathbf{f}_{\text{drag}} &= -8\pi\eta D \mathbf{v}_{\text{swim}} (1.0276 + 0.3963(H/D) \\ &\quad - 0.0259(H/D)^2 + 0.0014(H/D)^3) \\ &= c_{\text{drag}} \mathbf{v}_{\text{swim}} \end{aligned} \quad (4)$$

where  $\eta$  is the viscosity of the fluid, and  $\mathbf{v}_{\text{swim}}$  is the swimming speed of the robot. The resistive fluidic drag torque due to the

rotational motion of the cylindrical body is approximated by the Stokes drag as

$$\mathbf{T}_{\text{drag}} = \pi\eta H D^2 \boldsymbol{\omega}. \quad (5)$$

For the magnetic body without any flagella attached to rotate with the applied rotating magnetic field in synchrony, the driving magnetic torque must balance the resistive torque on the body:

$$\mathbf{T}_m + \mathbf{T}_{\text{drag}} = \mathbf{0}. \quad (6)$$

Therefore, from (3) and (5), we can obtain the minimum magnetic field required to rotate a robot body with determined geometry at any given frequency, or we can design the robot body dimensions, given a rotation speed and magnetic field strength.

### C. Propulsive Force and Fluidic Drag Torque From the Flexible Flagellum

When the robot body is rotated by the applied magnetic field about its body axis, it conveys the rotation to the attached flagella that are originally straight. These rotating flagella then experience drag forces from the surrounding viscous fluid as a result of their relative movements to the background fluid. Due to the flexibility of the flagella, they can bend into chiral shapes under these drag forces and, thus, produce net thrust. To simplify the problem, we focus on a single flagellum without considering the hydrodynamic interactions between multiple flagella [50]. Under such an assumption, the total propulsive force or fluidic drag torques of multiple flagella are just linear sum of those generated by each single flagellum. We are also only interested in steady-state motions, and hence, the model would be time invariant. Further ignoring the hydrodynamic interactions between distant parts of the flagellum, the resistive-force theory gives the viscous drag force per unit length as

$$\mathbf{f}_{\text{vis}} = - [\xi_{\perp} (\mathbf{I} - \mathbf{r}_s \otimes \mathbf{r}_s) + \xi_{\parallel} \mathbf{r}_s \otimes \mathbf{r}_s] \mathbf{u}_{\text{fg}} \quad (7)$$

where  $\mathbf{r}(s)$  is the position vector at arc-length  $s$  and  $\mathbf{u}_{\text{fg}}(s)$  is the velocity of the flagellum at  $s$  relative to the background flow  $\mathbf{v}_b$ . If the hydrodynamic interactions between the body and the flagellum are further ignored for simplification and the fluid at distance is assumed quiescent, then  $\mathbf{u}_{\text{fb}} = \omega \hat{\mathbf{z}} \times \mathbf{r}$ .  $\xi_{\perp}$  and  $\xi_{\parallel}$  are the normal and tangential drag coefficients given approximately by resistive-force theory as [51]

$$\xi_{\perp} = \frac{4\pi\eta}{\log(L/a) + 1/2}, \text{ and } \xi_{\parallel} = \frac{2\pi\eta}{\log(L/a) - 1/2} \quad (8)$$

where  $a$  is the radius of a flagellum with circular cross section. Since the flagella on the robots have rectangular cross sections instead of circular, an effective radius that gives the same cross-sectional area is used to approximate the drag coefficients:

$$a_{\text{eff}} = \sqrt{\frac{b \times w}{\pi}}. \quad (9)$$

Since the swimming robot operates inside a container instead of an open space, wall effects are also considered as the

coefficients are multiplied by a correction term of [25]

$$\frac{\xi^*}{\xi_\infty} = \left(1 - \frac{2.1044\xi_\infty L}{6\pi\eta h}\right)^{-1} \quad (10)$$

where  $\xi_\infty$  is the drag coefficient without presence of walls,  $\xi^*$  is the drag coefficient adjusted for wall effects, and  $h$  is the distance to the walls. The bending force for the elastic flagellum is given by

$$\mathbf{F}_{\text{bend}} = -A \frac{\partial^3 \mathbf{r}}{\partial s^3} \quad (11)$$

where  $A$  is the bending stiffness of the flagellum. Ignoring the body weight of the flagellum, the steady-state shape of the bent flagella is determined by balance of viscous and elastic forces,  $\partial \mathbf{F}_{\text{bend}} / \partial s + \mathbf{f}_{\text{vis}} = \mathbf{0}$ , which gives the governing equation of elastohydrodynamics as

$$[\xi_\perp (\mathbf{I} - \mathbf{r}_s \otimes \mathbf{r}_s) + \xi_\parallel \mathbf{r}_s \otimes \mathbf{r}_s] \mathbf{u}_{\text{fg}} = -A \frac{\partial^4 \mathbf{r}}{\partial s^4}. \quad (12)$$

The boundary conditions are 1) at the attached end,  $\mathbf{r}(0) = (s_0, 0, 0)$  and  $\mathbf{r}_s(0) = \hat{x} \sin \theta_f + \hat{z} \cos \theta_f$ , where  $\hat{x}$  and  $\hat{z}$  are unit vectors in  $x$ - and  $z$ -directions, respectively; and 2) at the free end, both elastic force and torque should be zero, which gives  $\mathbf{r}_{ss}(L) = 0$  ( $\mathbf{r}_{ss} = \partial^2 \mathbf{r} / \partial s^2$ ) and  $\mathbf{r}_{sss}(L) = 0$  ( $\mathbf{r}_{sss} = \partial^3 \mathbf{r} / \partial s^3$ ).

Equation (12) can be solved numerically by the shooting method to find the steady-state shape  $\mathbf{r}$  of the rotating flagellum [52]. In addition, the propulsive force generated by the deformed flagellum can be obtained from the solution as  $\mathbf{f}_p = -\mathbf{F}_{\text{bend}}(0) \cdot \hat{z}$ , and the viscous torque experienced by the whole flagellum is  $\mathbf{T}_f = -A \hat{z} \cdot \mathbf{r}_s \times \mathbf{r}_{ss}(0) + \hat{z} \cdot \mathbf{F}_{\text{bend}} \times \mathbf{r}(0)$ .

When the robot body diameter is large or when the rotation frequency is high, the flow generated by the body's rotation would be significant, hence altering the hydrodynamics on the flagella. A further modification to the previous introduced model can be made to preliminarily examine the effect of hydrodynamic interactions between the robot body and the flagellum when the deflection of flagellum is not significant. The rotational motion of the body induces a rotational flow field around it, and the attached flagellum is also affected by this flow field as the relative velocity of the flagellum to the background fluid is changed. To simplify the problem, we consider a rotational flow field induced by an infinitely long cylinder to approximate the actual flow field:

$$\mathbf{v}_b = \omega \frac{(D/2)^3}{l^2} \hat{z} \times \mathbf{e}_l \quad (13)$$

where  $l$  is the distance from the axis of the cylinder to the point of interest, and  $\mathbf{e}_l$  is the unit vector in the direction of  $l$ . Such an approximation would result in a stronger flow field in the vicinity of the flagellum than the actual field, especially at the far end away from body, and thus, the propulsive force derived would give a lower bound to the actual propulsive force. Such inclusion of influence of body rotation was only applied to analyze the flagella that are slightly bent during rotation.

#### D. Swimming Speed

When the robot is swimming with a steady-state speed, the total forces and torques that it experiences should vanish such that

$$\mathbf{f}_p + \mathbf{f}_{\text{drag}} = \mathbf{0} \quad (14)$$

and

$$\mathbf{T}_m + \mathbf{T}_{\text{drag}} + \mathbf{T}_f = \mathbf{0}. \quad (15)$$

Equation (15), together with (3), gives the requirement on the strength of the applied magnetic field to rotate the swimming robot in synchrony with the rotating field. In addition, by solving (14) numerically, we can find the value of steady-state swimming speed  $|\mathbf{v}_{\text{swim}}|$  for every rotation frequency  $f$ . The comparison between numerical solutions and experimental result will be presented in Section IV-A.

#### E. Flagellum Geometry Analysis and Optimization

The previously established model can be used to find the optimal design of flagellum for the swimming robots. There are various parameters of a flagellum that can be modified, among which the major ones that are easy to adjust are length of the flagella  $L$ , anchoring tilt angle at the base  $\theta_f$ , connection offset distance  $s_0$ , and the material elastic modulus  $E$ . These parameters could have significant influences on the resulting propulsive force and fluidic drag torque. To find a flagellum design that generates large propulsive force, we first look at how each of these four parameters individually influences propulsive force by varying only one parameter at a time while keeping others constant, and examine the output propulsive forces from numerical calculation. Such results are plotted in Fig. 2(a)–(d), where each subplot shows how the propulsive force generated changes as the value of each of the four parameters varies. It is observed that  $f_p$  increases monotonically as  $s_0$  increases. For the other three parameters,  $f_p$  shows a peaking behavior as the parameters increase. This means that an optimization search on  $L$ ,  $E$ , and  $\theta_f$  would be necessary. To find the optimal design that gives a global maximum of propulsive force, the *patternsearch* function built in *MATLAB*, which finds minimum of function using pattern search algorithm, was applied with four input variables  $L$ ,  $E$ ,  $\theta_f$ , and  $s_0$ . The stopping criteria for the search function were set as a minimum tolerance of  $10^{-12}$  for the objective function. It should be noted that although  $f_p$  increases with  $s_0$ , the minimum robot body diameter  $D$  required to provide such  $s_0$  becomes larger as well. Therefore, according to (4), the smallest possible  $c_{\text{drag}}$  also increases, resulting in a less-significant change in swimming speed. This influence of  $c_{\text{drag}}$  is also considered during the search for the optimal flagellum, and the optimization goal is modified so as to find the largest  $f_p/c_{\text{drag}}$  based on the smallest possible  $c_{\text{drag}}$ . The optimization search was carried out for two different flagellum cross-sectional geometries:  $120 \mu\text{m}$  ( $w$ )  $\times$   $100 \mu\text{m}$  ( $b$ ) and  $60 \mu\text{m}$  ( $w$ )  $\times$   $50 \mu\text{m}$  ( $b$ ). All of the calculations assume the surrounding fluid has a dynamic viscosity of  $0.343 \text{ N}\cdot\text{s}\cdot\text{m}^{-2}$ , so as to keep  $\text{Re}$  far below unity. The range of rotation frequency  $f$  in which the optimization search was carried out was from 0 to 15 Hz. The

TABLE I  
OPTIMAL FLAGELLUM DESIGN FOR CROSS-SECTIONAL GEOMETRY OF  $120 \mu\text{m}$  ( $w$ ) $\times$  $100 \mu\text{m}$  ( $b$ )

Rotation frequency $f$	Flagellum $L$	Flagellum $E$	$\theta_f$	$s_0$	$f_p$	$T_f$
15 Hz	2.2 mm	10 MPa	$53^\circ$	$0 \mu\text{m}$	$4.79 \mu\text{N}$	$5.78 \times 10^{-5} \text{N}\cdot\text{m}$

TABLE II  
OPTIMAL FLAGELLUM DESIGN FOR CROSS-SECTIONAL GEOMETRY OF  $60 \mu\text{m}$  ( $w$ ) $\times$  $50 \mu\text{m}$  ( $b$ )

Rotation frequency $f$	Flagellum $L$	Flagellum $E$	$\theta_f$	$s_0$	$f_p$	$T_f$
15 Hz	1.1 mm	10 MPa	$53^\circ$	$0 \mu\text{m}$	$1.15 \mu\text{N}$	$0.71 \times 10^{-5} \text{N}\cdot\text{m}$

TABLE III  
OPTIMAL FLAGELLUM DESIGN FOR CROSS-SECTIONAL GEOMETRY OF  $100 \text{nm}$  ( $w$ ) $\times$  $100 \text{nm}$  ( $b$ )

Rotation frequency $f$	Flagellum $L$	Flagellum $A$	$\theta_f$	$s_0$	$f_p$	$T_f$
30 Hz	$3.72 \mu\text{m}$	$3.6 \times 10^{-24} \text{Nm}^2$	$52.90^\circ$	$0 \mu\text{m}$	$9.78 \times 10^{-14} \text{N}$	$1.13 \times 10^{-18} \text{N}\cdot\text{m}$

ranges of  $L$ ,  $E$ ,  $\theta_f$ , and  $s_0$  within which the optimization search was carried out were [0.3 mm, 2.5 mm] for  $L$ , [0.05 MPa, 10 MPa,] for  $E$ , [ $0^\circ$ ,  $70^\circ$ ] for  $\theta_f$ , and [0, 200  $\mu\text{m}$ ] for  $s_0$ . The results are listed in Tables I and II.

Optimization results show that the optimal flagellum would be anchored on the rotation axis of the robot body with zero offset, i.e.,  $s_0 = 0$ . In that case, the maximum swimming speed would be achieved by attaching the flagellum to a robot body with diameter  $D = w$ . The maximum swimming speed achievable at  $f = 15 \text{ Hz}$  would be about 12 mm/s for  $w = 120 \mu\text{m}$  and 5 mm/s for  $w = 60 \mu\text{m}$ . Such performance is comparable with the existing microswimmers [31]. However, according to (3), to provide enough driving torque to rotate such optimal flagellum with the hardware currently available, the aspect ratio of the body needs to be greater than 20:1, and hence, the fabrication of such body would be difficult. Therefore, in this study, we did not adopt the optimal flagellum design. However, the optimization does give insight to how large an  $f_p$  we could possibly obtain by varying flagellum geometry and could be beneficial to the design of flagellum.

Although we only applied the previous models on mesoscale robot prototypes, they are also valid for micrometer-scale swimmers using single or multiple flexible straight tails. Therefore, the optimization process can also be performed for micrometer-scale swimming robots. As a demonstration, we additionally performed the optimization for a flagellum with cross-sectional dimensions of  $100 \text{ nm} \times 100 \text{ nm}$ , and the result is listed in Table III. The optimization assumed an aquatic environment of a dynamic viscosity of  $0.001 \text{ N}\cdot\text{s}\cdot\text{m}^{-2}$ , with the range of rotation frequency  $f$  to be from 1 to 30 Hz. In this optimization, we set the bending stiffness of the flagellum to  $3.6 \times 10^{-24} \text{ N}\cdot\text{m}^2$  [31], because at such a small scale, the bending stiffness calculated by material's bulk modulus could be much higher than the actual value. The ranges of  $L$ ,  $\theta_f$ , and  $s_0$  within which the optimization search was carried out were [0.5  $\mu\text{m}$ , 15  $\mu\text{m}$ ] for  $L$ , [ $0^\circ$ ,  $70^\circ$ ] for  $\theta_f$ , and [0, 2  $\mu\text{m}$ ] for  $s_0$ . We assume that the flagellum rotates near a bottom surface (5  $\mu\text{m}$  above it), where such wall effect phenomenon has been observed typically in swimming of not neutrally buoyant or magnetically nonlevitated microswimmers [26], [29], [31]. The underlying surface acts to increase hydrodynamic drag on the flagellum and, hence, the propulsive force. The optimization result is listed in Table III. It is estimated that the swimming speed of a swimming microrobot with this

optimized flagellum attached to a  $1.5 \mu\text{m}$  ( $H$ )  $\times$   $200 \text{ nm}$  ( $D$ ) cylindrical body is about 22  $\mu\text{m/s}$  at 30 Hz, which surpasses that of the existing artificial microswimmers in the literature [31].

#### F. Flagellum With Intrinsic Planar Curvatures

As another design variable and a significant advantage, the proposed fabrication method is capable of fabricating flagella that have much more complex planar shapes other than the simple straight shape. Therefore, it would be helpful if we can model the bending behavior of flexible flagella that have intrinsic planar curvatures and exam the hydrodynamics, like we have done for the straight ones. We achieved this based on the previous numerical model of the straight and flexible flagellum, but with additional modifications to capture the intrinsic curvatures of the nonstraight flagella. The following iteration is established to model the bending of a nonstraight flagellum. 1) The original curved flagellum is divided into  $N_c$  consecutive segments, labeled from first to  $N_c^{\text{th}}$  between the anchoring point of the flagellum on the body ( $s = 0$ ) and the free end ( $s = L$ ). Each segment is treated as a short, straight, and flexible flagellum that is fixed at one end and free at the other. 2) The boundary conditions at  $s = 0$  of the original curved flagellum is applied onto the first segment with a set of guessed boundary conditions applied on the free end, and then the same governing equations, (12) is solved for this segment. 3) The solutions of  $\mathbf{r}$ ,  $\mathbf{r}_{ss}$ , and  $\mathbf{r}_{sss}$  at the free end of the  $(k - 1)^{\text{th}}$  segment, with  $k = 2, 3, \dots, N_c$ , are directly applied as the boundary conditions at the fixed end for the  $k^{\text{th}}$  segment, while  $\mathbf{r}_s$  is revised to capture the intrinsic curvature of the original flagellum and then added to the boundary conditions. 4) Equation (12) is then solved for the  $k^{\text{th}}$  segment. 5) A shooting method as previously introduced is used, iterating from steps 1 to 4, to finally obtain a set of solutions for the  $N_c^{\text{th}}$  segment at the free end that matches the boundary conditions of the original flagellum at  $s = L$ . One key step to establish the numerical model for nonstraight flagellum is to modify  $\mathbf{r}_s$  in step 3 of the above iteration to capture the intrinsic curvature of the curved flagellum. This is accomplished by applying to  $\mathbf{r}_s$  a rotation transformation between the tangential vector at the free end of the deformed  $(k - 1)^{\text{th}}$  segment and the tangential vector at the fixed end of the  $k^{\text{th}}$  segment from the original, undeformed flagellum:

$$\mathbf{r}_s^r = \mathbf{T}_r \mathbf{r}_s^{\text{on}} \quad (16)$$

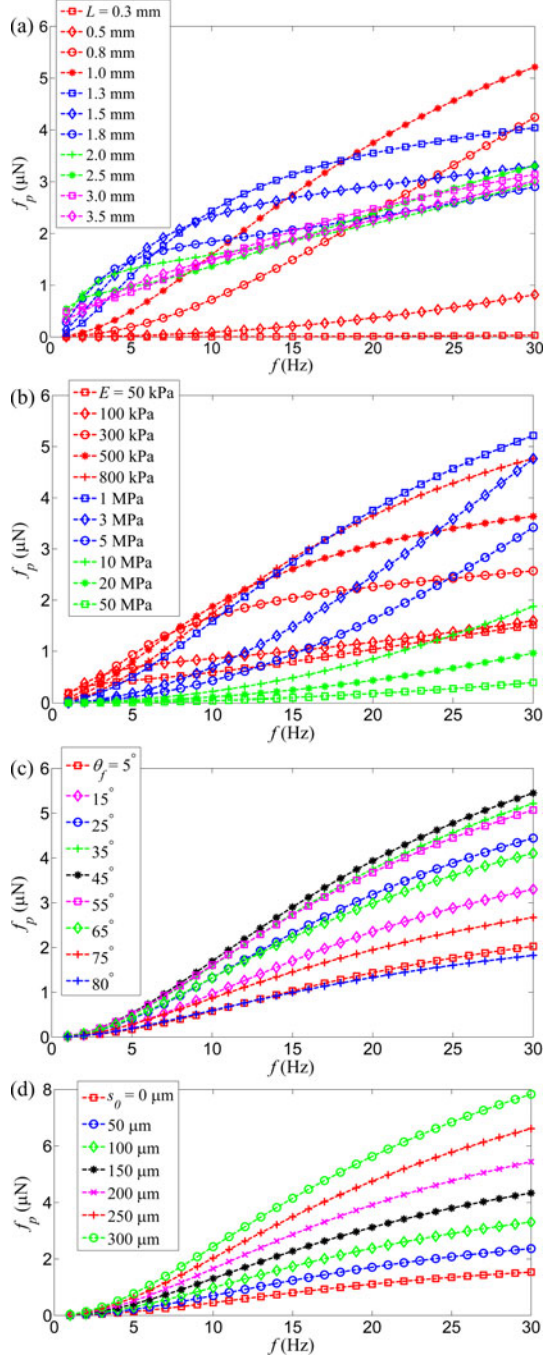


Fig. 2. Simulation results to show the influence of  $L$ ,  $E$ ,  $\theta_f$ , and  $s_0$  on propulsive force. Propulsive force results as a function of rotation frequency when (a) changing only  $L$ , with  $E = 1$  MPa,  $\theta_f = 35^\circ$ , and  $s_0 = 190$   $\mu\text{m}$ ; (b) changing only  $E$ , with  $L = 1$  mm,  $\theta_f = 35^\circ$ , and  $s_0 = 190$   $\mu\text{m}$ ; (c) changing only  $\theta_f$ , with  $L = 1$  mm,  $E = 1$  MPa, and  $s_0 = 190$   $\mu\text{m}$ ; and (d) changing only  $s_0$ , with  $L = 1$  mm,  $E = 1$  MPa, and  $\theta_f = 35^\circ$ .

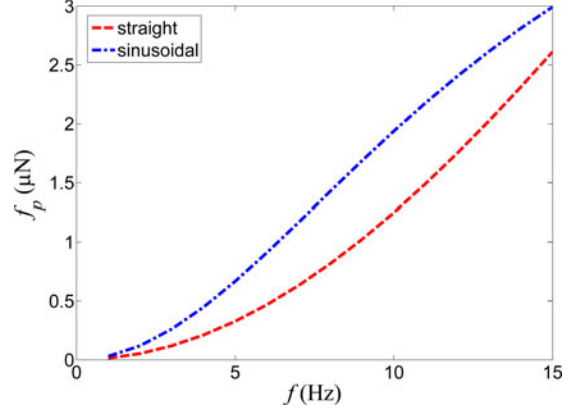


Fig. 3. Comparison between the propulsive force ( $f_p$ ) generated by a sinusoidal flagellum and a straight flagellum that differ in shape as a function of rotation frequency. Both results are numerical solutions from the models established in this study.

with (17), shown at the bottom of the page, and

$$\hat{\mathbf{r}} = \mathbf{r}_s^{op} \times \mathbf{r}_s^s \quad (18)$$

$$\varphi_r = \arccos \left( \frac{\mathbf{r}_s^{op} \cdot \mathbf{r}_s^s}{|\mathbf{r}_s^{op}| |\mathbf{r}_s^s|} \right) \quad (19)$$

where  $\mathbf{r}_s^r$  is the revised  $\mathbf{r}_s$  for the  $k^{\text{th}}$  segment,  $\mathbf{r}_s^{op}$  and  $\mathbf{r}_s^{on}$  are  $\mathbf{r}_s$  calculated from the original flagellum before deformation of the  $(k-1)^{\text{th}}$  and  $k^{\text{th}}$  segment, respectively, and  $\mathbf{r}_s^s$  is  $\mathbf{r}_s$  at the free end from solutions of the  $(k-1)^{\text{th}}$  segment,  $k = 2, 3, \dots, N_c$ .  $\hat{\mathbf{r}}_i$  with  $i = x, y, z$  denotes the  $i$  component of vector  $\hat{\mathbf{r}}$ .

The established model was solved for a flagellum of planar sinusoidal shape. The peak amplitude of the sinusoidal curve is 75  $\mu\text{m}$ , and there are 3.5 wavelengths within the flagellum with a length of 1500  $\mu\text{m}$ . The propulsive force generated by this nonstraight flagellum was compared with the force generated by a straight flagellum that has the same effective length, the same anchoring angle  $\theta_f$ , and the same bending modulus. The results are plotted in Fig. 3. It is observed that, theoretically, an improvement can be achieved in propulsive force generation by having a more complex planar curvature in the flexible flagellum.

### III. EXPERIMENTAL SETUP AND SWIMMING ROBOT FABRICATION

A six-coil electromagnetic-coil system was used to generate a uniform rotating magnetic field in the workspace [53]. The maximum field strength this system can generate is about 12 mT, with 6% uniformity over a 30-mm space.

$$\mathbf{T}_r = \begin{bmatrix} \frac{\hat{r}_x^2 + (\hat{r}_y^2 + \hat{r}_z^2) \cos \varphi_r}{|\hat{\mathbf{r}}|^2} & \frac{\hat{r}_x \hat{r}_y (1 - \cos \varphi_r) - \hat{r}_z |\hat{\mathbf{r}}| \sin \varphi_r}{|\hat{\mathbf{r}}|^2} & \frac{\hat{r}_x \hat{r}_z (1 - \cos \varphi_r) + \hat{r}_y |\hat{\mathbf{r}}| \sin \varphi_r}{|\hat{\mathbf{r}}|^2} \\ \frac{\hat{r}_x \hat{r}_y (1 - \cos \varphi_r) + \hat{r}_z |\hat{\mathbf{r}}| \sin \varphi_r}{|\hat{\mathbf{r}}|^2} & \frac{\hat{r}_y^2 + (\hat{r}_x^2 + \hat{r}_z^2) \cos \varphi_r}{|\hat{\mathbf{r}}|^2} & \frac{\hat{r}_y \hat{r}_z (1 - \cos \varphi_r) - \hat{r}_x |\hat{\mathbf{r}}| \sin \varphi_r}{|\hat{\mathbf{r}}|^2} \\ \frac{\hat{r}_x \hat{r}_z (1 - \cos \varphi_r) - \hat{r}_y |\hat{\mathbf{r}}| \sin \varphi_r}{|\hat{\mathbf{r}}|^2} & \frac{\hat{r}_y \hat{r}_z (1 - \cos \varphi_r) + \hat{r}_x |\hat{\mathbf{r}}| \sin \varphi_r}{|\hat{\mathbf{r}}|^2} & \frac{\hat{r}_z^2 + (\hat{r}_x^2 + \hat{r}_y^2) \cos \varphi_r}{|\hat{\mathbf{r}}|^2} \end{bmatrix} \quad (17)$$

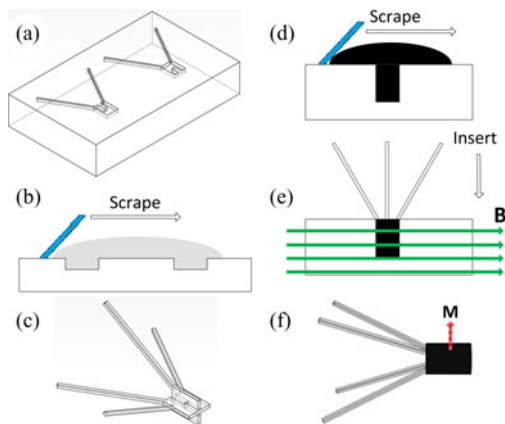


Fig. 4. Fabrication procedure for the miniature swimming robots with multiple flexible flagella. *Step 1*: (a) Flexible negative mold for the planar parts is fabricated via a typical soft-lithography process. (b) Planar parts are fabricated through a micromolding process. (c) Such planar parts are assembled manually into 3-D structures. *Step 2*: (d) Mixture of magnetic particles (NdFeB) and polyurethane is poured into the cylindrical cavities on another negative mold. (e) Assembly is vertically inserted into the filled cavities and left to cure. During curing, a horizontal magnetic field is applied to magnetize the robot body in the direction perpendicular to its long axis. (f) Molded robot with multiple flagella is peeled from the mold.

Fabricated miniature swimming robots in this study consist of two parts: a magnetic body that can respond to an externally applied magnetic field for actuation and control and flexible flagella, which act as the propulsive element during swimming. Three-dimensional microstructures are necessary in order to equip the robots with multiple flexible and tilted flagella, and thus, conventional single step 2-D lithography-based fabrication techniques would not be adequate [54]. Therefore, our swimming robots were fabricated by a two-step micromolding process (see Fig. 4), which is based on simple and inexpensive planar photolithography methods, micromolding, and manual assembly. The first step was a typical soft-photolithography-based micromolding process: Photolithography was first used to transfer the desired planar patterns that have notches at desired positions for assembling to the SU-8 photoresist substrate; then, a mold-making elastomer (silicone rubber, Dow Corning HS II RTV, or polydimethylsiloxane, Dow Corning Sylgard 184) was poured over the patterned substrate to form a negative mold; the planar parts, which are made of polymer (ST-1060 or ST-1087, BJB Enterprises), were cured and pulled off from the negative mold. After the planar parts were fabricated, we manually assembled them into 3-D shapes, each consisting of two to three (only for robots with six flagella) planar parts. Afterward, a mixture of NdFeB permanent magnet particles (MQP-15-7, Magnequench) and polyurethane (TC-892, BJB Enterprises) was poured into another negative rubber mold with blind-ended cylindrical cavities, prepared via a process similar to the first step but using a multicoating technique to build up a SU-8 layer of 600- $\mu\text{m}$  thickness. The assemblies were then inserted vertically into the cavities filled with magnetic mixture and allowed to cure for the final 3-D shapes. The walls of the cavities as well as the high viscosity of the magnetic mixture helped to maintain the vertical postures of the inserted assemblies. During curing, the negative rubber mold was exposed under a strong horizontal

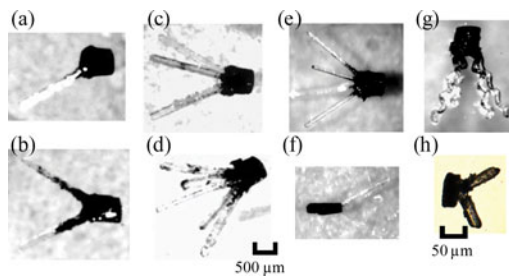


Fig. 5. Optical microscope images of fabricated miniature swimming robots with different designs. (a)–(d) Robots with a cylindrical body of  $500\ \mu\text{m}$  ( $D$ ) $\times$  $600\ \mu\text{m}$  ( $H$ ) and flagella of  $120\ \mu\text{m}$  ( $w$ ) $\times$  $100\ \mu\text{m}$  ( $b$ ) $\times$  $1.5\ \text{mm}$  ( $L$ ) made of ST-1087 (BJB Enterprises,  $E = 9.8\ \text{MPa}$ ). (e) Robot with a cylindrical body of  $500\ \mu\text{m}$  ( $D$ ) $\times$  $600\ \mu\text{m}$  ( $H$ ), and flagella of  $60\ \mu\text{m}$  ( $w$ ) $\times$  $50\ \mu\text{m}$  ( $b$ ) $\times$  $1\ \text{mm}$  ( $L$ ) made of ST-1060 (BJB Enterprises,  $E = 2.9\ \text{MPa}$ ). (f) Robot with a cylindrical body of  $180\ \mu\text{m}$  ( $D$ ) $\times$  $700\ \mu\text{m}$  ( $H$ ), and flagella of  $60\ \mu\text{m}$  ( $w$ ) $\times$  $50\ \mu\text{m}$  ( $b$ ) $\times$  $1\ \text{mm}$  ( $L$ ) made of ST-1060 ( $E = 2.9\ \text{MPa}$ ). (g) Robot with a cylindrical body of  $500\ \mu\text{m}$  ( $D$ ) $\times$  $600\ \mu\text{m}$  ( $H$ ), and sinusoidal flagella made of ST-1087 ( $E = 9.8\ \text{MPa}$ ). (h) Robot with two flagella that has a cylindrical body of  $50\ \mu\text{m}$  ( $D$ ) $\times$  $50\ \mu\text{m}$  ( $H$ ) and a total length of  $90\ \mu\text{m}$ .

magnetic field to magnetize the magnetic robot bodies in the direction perpendicular to their axes.

The fabricated swimming robots with straight and flexible flagella can be grouped into three different sets of dimensions and materials. Set I [see Fig. 5(a)–(d)] has a cylindrical body of  $500\ \mu\text{m}$  (diameter,  $D$ ) $\times$  $600\ \mu\text{m}$  (height,  $H$ ), and flagella of  $120\ \mu\text{m}$  (width,  $w$ ) $\times$  $100\ \mu\text{m}$  (thickness,  $b$ ) $\times$  $1.5\ \text{mm}$  (length,  $L$ ) made of ST-1087 (Young's modulus of  $9.8\ \text{MPa}$ , e.g.,  $E = 9.8\ \text{MPa}$ ). Set II [see Fig. 5(e)] has the same cylindrical body as Set I, but with flagella of  $60\ \mu\text{m}$  ( $w$ ) $\times$  $50\ \mu\text{m}$  ( $b$ ) $\times$  $1\ \text{mm}$  ( $L$ ) made of ST-1060 ( $E = 2.9\ \text{MPa}$ ). Set III [see Fig. 5(f)] has a cylindrical body of  $180\ \mu\text{m}$  ( $D$ ) $\times$  $700\ \mu\text{m}$  ( $H$ ) and flagella of  $60\ \mu\text{m}$  ( $w$ ) $\times$  $50\ \mu\text{m}$  ( $b$ ) $\times$  $1\ \text{mm}$  ( $L$ ) made of ST-1060. Besides straight flagella, robots with four planar sinusoidal flagella [see Fig. 5(g)] were also fabricated to demonstrate the capability of the proposed fabrication method for creating more complex flagella shapes.

Robots with even smaller body diameter, about  $100\ \mu\text{m}$ , could be fabricated using the same process, but guaranteeing the manual assembly precision would be more challenging. Avoiding such a manual assembly process step, swimming robots with up to two artificial flagella that are under  $100\ \mu\text{m}$  in length and several tens of micrometers in diameter can still be fabricated via the proposed fabrication process. As a demonstration, a swimming microrobot with two straight flexible flagella that is about  $90\ \mu\text{m}$  long and has a body diameter of  $50\ \mu\text{m}$  was fabricated [see Fig. 5(h)]. For microswimmers that are less than  $10\ \mu\text{m}$  in size, there are existing techniques that can be adopted to fabricate multiflagellated robots, such as multiphoton lithography [55] and self-scrolling or self-folding [26], [56].

#### IV. EXPERIMENTAL RESULTS AND DISCUSSION

All experiments were carried out in a cylindrical open-top container with an inner diameter of  $33\ \text{mm}$  and a height of  $37\ \text{mm}$ , filled with silicone oils. Actuation of the swimming robots was realized by the rotating magnetic field of  $|\mathbf{B}| = 12\ \text{mT}$  generated by the electromagnetic-coil system with iron

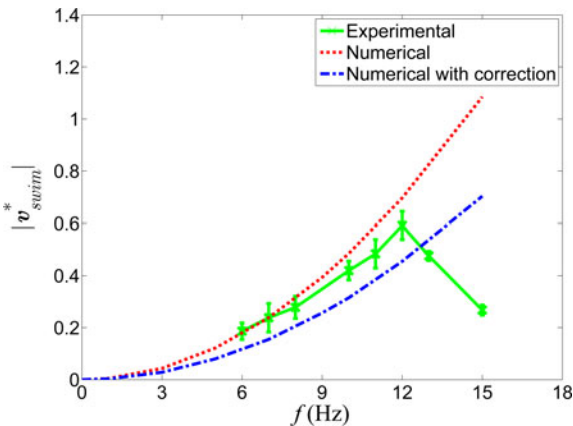


Fig. 6. Comparison between the swimming speeds solved from the original model, the modified model that includes the body influence, and those obtained experimentally at various rotation frequencies. The swimming speeds are normalized to  $|v_{swim}^*|$  by the robot body height  $H$  of  $600 \mu\text{m}$ .

cores inserted into the coils to magnify the field. Three velocity measurements were taken for each set of data, and the error bars on the result plots indicate standard deviation of the measured values. The position differentiated over time was used to calculate the average swimming speed of a robot.

#### A. Verification of the Established Model

An experiment was carried out to examine the validity of previously established single-flagellum model. The comparison of swimming speeds of a single-flagellum swimming robot that were solved from the original model, the model modified with body rotation and obtained from experiments, is illustrated in Fig. 6. The robot's parameters are listed in Table IV. All the swimming speed data were normalized by the robot body height  $H$ , which is  $600 \mu\text{m}$ . In the experimental result, the swimming speed drops after the rotation frequency reaches 12 Hz because the rotation of robot body steps out of synchrony with the rotating magnetic field due to lack of enough driving torque.

The comparison shows that the solutions from both models bound the experimental measurements well. This demonstrates that, in the small-deformation case, the original model would give an upper bound to the swimming speed of the miniature swimming robot, while the modified model would give a lower bound.

#### B. Effect of Number of Artificial Flagella

Swimming speed measurements were taken on the Set I miniature swimming robots in a silicone oil of 350 cSt viscosity ( $\text{Re} \sim 10^{-3}$ ), and the results are plotted in Fig. 7. It is observed that the swimming speed is significantly improved by increasing the number of attached flagella ( $N_{fl}$ ) from one to four. The swimming speed is linearly increasing with  $N_{fl}$ . However, as the number of flagella increases to six, the resulting swimming speed decreases significantly. This may be due to the hydrodynamic interactions between flagella becoming stronger as the spacing between flagella becomes smaller when the number of flagella increases. Each flagellum is affected by

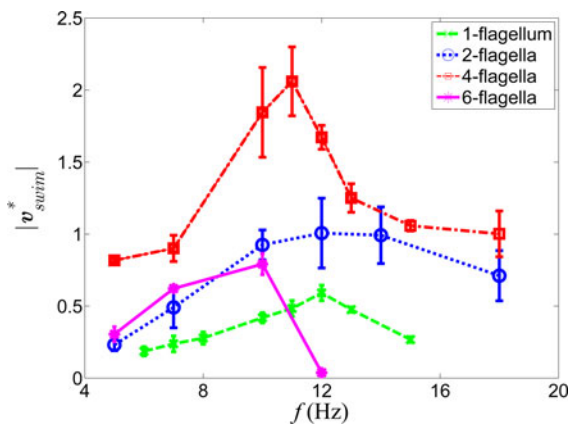


Fig. 7. Experimental comparison on swimming speed as a function of rotation frequency of swimming robots with one, two, and four artificial flagella in Set I dimension (Robot body:  $500 \mu\text{m}$  ( $D$ ) $\times 600 \mu\text{m}$  ( $H$ ); flagella:  $120 \mu\text{m}$  ( $w$ ) $\times 100 \mu\text{m}$  ( $b$ ) $\times 1.5 \text{ mm}$  ( $L$ ), and  $E = 9.8 \text{ MPa}$ ,  $\theta_f = 35^\circ$ , and  $s_0 = 190 \mu\text{m}$ ).  $|v_{swim}^*|$  is the swimming speed,  $|v_{swim}|$ , normalized by the robot body height  $H$  of  $600 \mu\text{m}$ .

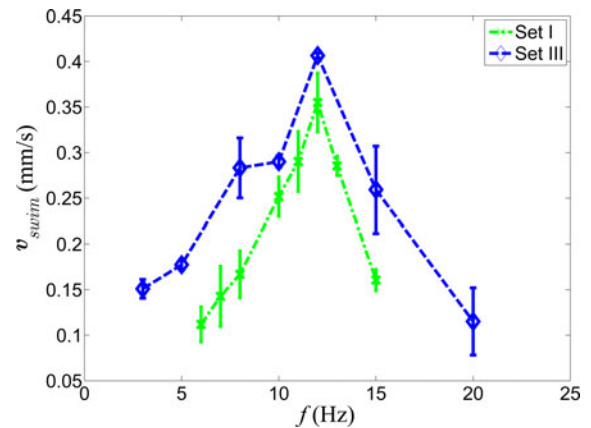


Fig. 8. Experimental comparison on swimming speed as a function of rotation frequency of single-flagellum swimming robots in Set I (Robot body:  $500 \mu\text{m}$  ( $D$ ) $\times 600 \mu\text{m}$  ( $H$ ); flagella:  $120 \mu\text{m}$  ( $w$ ) $\times 100 \mu\text{m}$  ( $b$ ) $\times 1.5 \text{ mm}$  ( $L$ ), and  $E = 9.8 \text{ MPa}$ ,  $\theta_f = 35^\circ$ , and  $s_0 = 190 \mu\text{m}$ ) and Set III (Robot body:  $180 \mu\text{m}$  ( $D$ ) $\times 700 \mu\text{m}$  ( $H$ ); flagella:  $60 \mu\text{m}$  ( $w$ ) $\times 50 \mu\text{m}$  ( $b$ ) $\times 1 \text{ mm}$  ( $L$ ), and  $E = 2.9 \text{ MPa}$ ,  $\theta_f = 35^\circ$ , and  $s_0 = 60 \mu\text{m}$ ).

the fluid flow generated by the motion of nearby flagella, and hence, the relative speed  $u_{fg}$  decreases. As a result, the propulsive force one flagellum can generate becomes much weaker than the force generated by isolated flagella, which leads to a slower swimming speed. The speed declines after certain  $f$ 's are the results of stepping out of synchronous rotation with the applied magnetic field.

#### C. Effect of Flagella Geometry and Reynolds Number

Comparisons of the swimming speed of swimming robots with single flagellum in Set I ( $L = 1.5 \text{ mm}$ ,  $E = 9.8 \text{ MPa}$ ,  $\theta_f = 30^\circ$ , and  $s_0 = 190 \mu\text{m}$ ) and Set III ( $L = 1 \text{ mm}$ ,  $E = 2.9 \text{ MPa}$ ,  $\theta_f = 35^\circ$ , and  $s_0 = 60 \mu\text{m}$ ) were also carried out, and the results are illustrated in Fig. 8. It can be seen that the swimming speed can be improved by varying the robot design, as analyzed in Section II-E. However, even if the dimensions

TABLE IV  
PARAMETERS OF THE SINGLE-FLAGELLUM ROBOT, THE STEADY-STATE SWIMMING SPEED OF WHICH WAS MEASURED EXPERIMENTALLY AS WELL AS SOLVED BY BOTH THE ORIGINAL MODEL AND MODEL WITH BACKGROUND FLOW MODIFICATION

Body $H$	Body $D$	Flagellum $L$	Flagellum $w$	Flagellum $b$	Flagellum $E$	$\theta_f$	$s_0$	$\eta$
600 $\mu\text{m}$	500 $\mu\text{m}$	1500 $\mu\text{m}$	120 $\mu\text{m}$	100 $\mu\text{m}$	9.8 MPa	30°	190 $\mu\text{m}$	0.343 Nsm <sup>-2</sup>

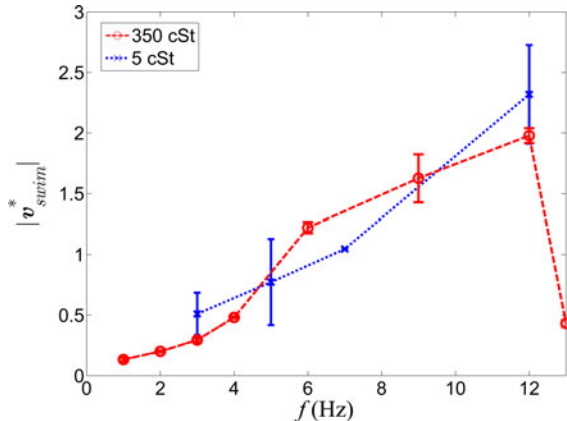


Fig. 9. Experimental comparison of swimming speed as a function of rotation frequency of swimming robots with four flagella in silicone oil with viscosities of 5 cSt and 350 cSt, respectively.

of the body and attached flagellum, as well as the material used for flagellum, are significantly changed, the swimming speed is improved only by a limited margin. In addition, even if the optimal design of flagella is used, by increasing the number of flagella can still significantly improve swimming performance, which is illustrated in Section IV-B. This demonstrates the advantage of having multiple artificial flagella on a swimming robot. Measurements were also taken for miniature swimming robots in Set II with four flagella in silicone oil with two different kinematic viscosities of 5 cSt and 350 cSt, respectively, and the results are plotted in Fig. 9. It is observed that even at mid Re environment (5 cSt oil, Re up to 0.5), the artificial flagella can still generate a strong enough propulsive force for the robot to swim. Therefore, the miniature swimming robots would be potentially capable to work in a wide range of fluids with different viscosities. A stepout was not observed in 5 cSt oil within the range of rotating frequency tested due to the low fluidic torque experienced by the robot in this less viscous fluid. However, a stepout is always expected but would be at a much higher frequency than that in the 350 cSt oil. Measurement in fluids with even lower viscosities, such as water, is not achievable in this study as the robot sinks too fast in such a fluid before any measurement on translational swimming speed can be taken in suspension. However, the mechanism is expected to work in water, and we also present a video demonstration from the top view of the miniature swimming robot swimming inside a water-filled glass tube with diameter of 5.5 mm. The video can be found in supplementary materials.

#### D. Flagella With More Complex Two-Dimensional Shape

As previously mentioned, the proposed fabrication method is capable of fabricating more complex planar shapes than the simple straight shape for flagella. Miniature robots with four sinusoidal flagella attached were fabricated, and their swim-

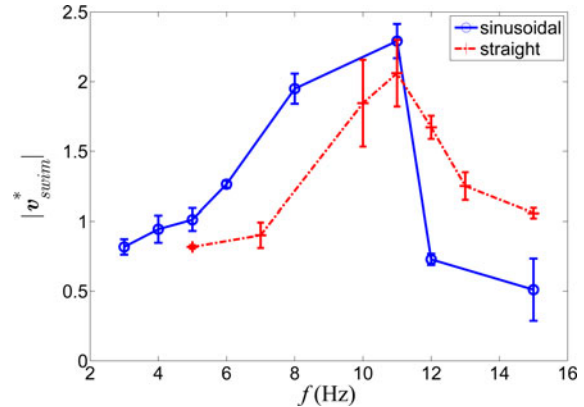


Fig. 10. Comparison of swimming speed as a function of rotation frequency of the miniature swimming robot with four straight and sinusoidal flagella, respectively.

ming speed in 350 cSt silicone oil was measured and compared with that of the robot in Set I with four straight flagella. Fig. 10 illustrates the experiment results. As predicted by the numerical simulation on single flagellum of Section II-F, the experimental results show that the swimming speed is improved by the sinusoidal shape of flagella. Therefore, the swimming performance could potentially benefit from a more complex flagella design. Considering that the fabrication process for flagella with a nonstraight 2-D shape is generally identical to the process for straight flagella with limited extra complexity, robots with non-straight flagella that may have a significantly improved swimming performance can be easily fabricated with the method proposed in this paper. This would be beneficial in the cases where a strong axial propulsive force is desired, such as swimming against slow flows or applying a pressure to the surrounding environment by the swimming robot. In addition, it is possible to locally and drastically adjust the intensity of hydrodynamic interactions between multiple attached flagella by changing the curvature design of them, which provides a potentially powerful tool to study the multiple-flagella hydrodynamic interaction.

#### E. Advantages and Limitations of Using Multiple Flagella

The experiment results demonstrated that multiple straight, flexible flagella could provide enhanced propulsion. Therefore, one significant advantage of using multiple flagella is that a much higher propulsive force, and, hence, the resulting swimming speed, can be achieved at a given rotation frequency. In other words, using multiple flagella lowers the rotation frequency required to achieve a desired swimming speed or propulsive force. This would be beneficial to potential future medical applications inside low velocity flows (urinary tract or capillaries) or stagnant fluid (spinal cord fluid, brain lobes, and inside the eye) regions inside the human body, because a lower frequency required for the driving magnetic field reduces the

technical challenges to design the field-generating device (either electromagnetic coils or permanent magnets). In addition, a stronger propulsion-generation capability gives the potentials of the swimming robots to operate fast to achieve medical tasks in a shorter duration. However, whether or not multiple artificial flagella can improve the maximum swimming speed  $\max|\mathbf{v}_{\text{swim}}|$  for miniature robots would need further analysis. While the propulsive force is improved by multiple flagella, the total viscous torque applied on these flagella also increases. As shown by experiments, when hydrodynamic interactions between multiple flagella are not significant, the swimming speed is almost linearly increased by the number of flagella ( $N_{fl}$ ). Therefore, it is reasonable to assume that the propulsive force and viscous torque also linearly increase with  $N_{fl}$ . Previous studies have shown that, for a single straight, flexible flagellum, the relationship between  $f_p$  generated and  $T_f$  required is  $(\log f_p \log T_f) > 1$  [39], [40], which indicates that  $f_p = k_{\text{const}} T_f^\beta$  with  $\beta > 1$ .

It is also observed in the experiments that when the rotation of robot steps out of synchrony with the rotating magnetic field, the robot begins to oscillate back and forth and its swimming speed begins to drop rapidly as the rotation frequency keeps rising. Therefore,  $\max|\mathbf{v}_{\text{swim}}|$  is reached right before stepping-out. Stepping-out occurs when the maximum magnetic torque that can be applied onto the robot is less than the driving torque required to rotate the robot at a given rotation frequency:  $|\mathbf{T}_{\text{max}}| < (|\mathbf{T}_{\text{drag}}| + T_f)$ . Therefore, given a limited applied  $\mathbf{B}$  magnitude, multiple flexible artificial flagella would lead to a significant improvement on  $\max|\mathbf{v}_{\text{swim}}|$  when  $|\mathbf{T}_{\text{drag}}| / (N_{fl} \cdot T_f) \gg 1$ . If  $T_f$  is comparable with  $|\mathbf{T}_{\text{drag}}|$ , then  $\max|\mathbf{v}_{\text{swim}}|$  of a multiflagella robot could be smaller than that of a single-flagella robot with the same flagella and robot body design. This could be a potential disadvantage of using multiple flagella. In our case, drag torque on the robot body dominates that on the flagella as the stepout frequencies of the robots do not change significantly with number of flagella, and hence, we did not experience this potential drawback.

## V. CONCLUSION AND FUTURE WORK

In this study, we have designed and fabricated miniature swimming robots with multiple (up to six) flexible flagella. Physical models were established, and numerical simulations were carried out to predict the swimming performance of the robots and guide the robot design. The fabrication process is inexpensive and relatively simple, including two steps of soft-lithography, micromolding, and manual assembly processes. Experimental results for robots with straight flexible flagella designs demonstrated that stronger propulsive force, and hence the resulting swimming speed of robots, could be achieved by increasing the number of artificial flagella at a given rotation frequency, as long as the hydrodynamic interactions between flagella are not so significant as to affect the swimming performance. The proposed fabrication method was also shown to be capable of creating more complicated planar flagella designs, such as sinusoidal curves, which may benefit propulsive force generation and swimming performance and could be potentially useful for more sophisticated tasks such as object transportation

or manipulation [48]. Increasing the number of artificial flagella has been shown as a promising way to improve swimming performance of miniature robots in fluidic environments with a wide range of viscosities. Future work includes neutrally buoyant robot body design and fabrication, fabrication of robots with even smaller size, and fabrication and characterization of flagella with shapes that would be potentially useful for specific applications, such as microobject manipulation and transportation. The use of the developed robots as micropumps or local fluid flow controllers inside microfluidic channels could also be a potential future application [16].

## REFERENCES

- [1] J. Edd, S. Payen, M. Stoller, B. Rubinsky, and M. Sitti, "Biomimetic propulsion mechanism for a swimming surgical micro-robot," in *Proc. IEEE/RSJ Int. Conf. Intell. Rob. Syst.*, Las Vegas, NV, USA, 2003, pp. 2583–2588.
- [2] B. Behkam and M. Sitti, "Design methodology for biomimetic propulsion of miniature swimming robots," *J. Dyn. Syst. Meas. Control Trans. ASME*, vol. 128, no. 1, pp. 36–43, 2006.
- [3] M. Sitti, "Voyage of the microrobots," *Nature*, vol. 458, pp. 1121–1122, 2009.
- [4] L. Zhang, K. Peyer, and B. J. Nelson, "Artificial bacterial flagella for micromanipulation," *Lab Chip*, vol. 10, no. 17, pp. 2203–2215, 2010.
- [5] B. J. Nelson, I. Kaliakatsos, and J. J. Abbott, "Microrobots for minimally invasive medicine," *Annu. Rev. Biomed. Eng.*, vol. 12, pp. 55–85, 2010.
- [6] M. Sitti, "Microscale and nanoscale robotics systems [grand challenges of robotics]," *IEEE Robot. Autom. Mag.*, vol. 14, no. 1, pp. 53–60, Mar. 2007.
- [7] D. Frutiger, K. Vollmers, B. E. Kratochvil, and B. J. Nelson, "Small, fast, and under control: Wireless resonant magnetic micro-agents," *Int. J. Robot. Res.*, vol. 29, no. 5, pp. 613–636, 2010.
- [8] C. Pawashe, S. Floyd, and M. Sitti, "Modeling and experimental characterization of an untethered magnetic micro-robot," *Int. J. Robot. Res.*, vol. 28, no. 8, pp. 1077–1094, 2009.
- [9] E. Diller, C. Pawashe, S. Floyd, and M. Sitti, "Assembly and disassembly of magnetic mobile micro-robots towards deterministic 2-D reconfigurable micro-systems," *Int. J. Robot. Res.*, vol. 30, no. 14, pp. 1667–1680, 2011.
- [10] C. Pawashe, S. Floyd, and M. Sitti, "Multiple magnetic microrobot control using electrostatic clamping," *Appl. Phys. Lett.*, vol. 94, pp. 161408-1–161408-3, 2009.
- [11] S. Floyd, C. Pawashe, and M. Sitti, "Two-dimensional contact and non-contact micromanipulation in liquid using an untethered mobile magnetic micro-robot," *IEEE Trans. Robot.*, vol. 25, no. 6, pp. 1332–1342, Dec. 2009.
- [12] Z. Ye, E. Diller, and M. Sitti, "Micro-manipulation using rotational fluid flows induced by remote magnetic micro-manipulators," *J. Appl. Phys.*, vol. 112, pp. 064912-1–064912-7, 2012.
- [13] E. Diller, J. Giltinan, and M. Sitti, "Independent control of multiple magnetic microrobots in three dimensions," *Int. J. Robot. Res.*, vol. 32, no. 5, pp. 614–631, 2013.
- [14] S. Floyd, E. Diller, C. Pawashe, and M. Sitti, "Control methodologies for a heterogeneous group of untethered magnetic micro-robots," *Int. J. Robot. Res.*, vol. 30, no. 13, pp. 1553–1565, 2011.
- [15] E. Diller, S. Floyd, C. Pawashe, and M. Sitti, "Control of multiple heterogeneous magnetic micro-robots in two dimensions," *IEEE Trans. Robot.*, vol. 28, no. 1, pp. 172–182, Feb. 2012.
- [16] E. Diller, S. Miyashita, and M. Sitti, "Remotely addressable magnetic composite micro-pumps," *RSC Adv.*, vol. 2, no. 9, pp. 3850–3856, 2012.
- [17] ICNIRP, "Guidelines for limiting exposure to time-varying electric, magnetic, and electromagnetic fields (up to 300 GHz)," *Health Phys.*, vol. 74, pp. 494–522, 1998.
- [18] J. Wang, "Can man-made nanomachines compete with nature biomotors?," *ACS Nano*, vol. 3, pp. 4–9, 2009.
- [19] T. Mirkovic, N. Zacharia, G. D. Scholes, and G. A. Ozin, "Nanolocomotion—Catalytic nanomotors and nanorotors," *ACS Nano*, vol. 4, pp. 159–167, 2010.
- [20] B. Behkam and M. Sitti, "Effect of quantity and configuration of attached bacteria on bacterial propulsion of microbeads," *Appl. Phys. Lett.*, vol. 93, pp. 223901-1–223901-3, 2008.

- [21] D. Kim, A. Liu, E. Diller, and M. Sitti, "Chemotactic steering of bacteria propelled microbeads," *Biomed. Microdev.*, vol. 14, no. 6, pp. 1009–1017, 2012.
- [22] B. Behkam and M. Sitti, "Bacterial flagella-based propulsion and on/off motion control of microscale objects," *Appl. Phys. Lett.*, vol. 90, pp. 023902-1–023902-3, 2007.
- [23] M. R. Edwards, R. Wright, and M. Sitti, "Three dimensional motion analysis of bacteria-driven microbeads near and away from walls," *Appl. Phys. Lett.*, vol. 102, 2013.
- [24] J. J. Abbott, K. Peyer, M. Lagomarsino, L. Zhang, I. Kaliakatsos, and B. J. Nelson, "How should microrobots swim?," *Int. J. Robot. Res.*, vol. 28, pp. 1434–1447, 2009.
- [25] C. Brennen and H. Winet, "Fluid mechanics of propulsion by cilia and flagella," *Annu. Rev. Fluid Mech.*, vol. 9, pp. 339–398, 1977.
- [26] L. Zhang, J. J. Abbott, L. Dong, B. E. Kratochvil, D. Bel, and B. J. Nelson, "Artificial bacterial flagella: Fabrication and magnetic control," *Appl. Phys. Lett.*, vol. 94, pp. 064107-1–064107-3, 2009.
- [27] A. Ghosh and P. Fischer, "Controlled propulsion of artificial magnetic nanostructured propellers," *Nano Lett.*, vol. 9, pp. 2243–2245, 2009.
- [28] R. Dreyfus, J. Baudry, M. Roper, M. Fermigier, H. Stone, and J. Bibette, "Microscopic artificial swimmer," *Nature*, vol. 437, pp. 862–865, 2005.
- [29] U. Cheang, D. Roy, J. Lee, and M. Kim, "Fabrication and magnetic control of bacteria-inspired robotic microswimmers," *Appl. Phys. Lett.*, vol. 97, pp. 213704-1–213704-3, 2010.
- [30] W. Gao, S. Sattayasamitsathit, K. Manesh, D. Weihs, and J. Wang, "Magnetically powered flexible metal nanowire motors," *J. Amer. Chem. Soc.*, vol. 132, pp. 14403–14405, 2010.
- [31] O. Pak, W. Gao, J. Wang, and E. Lauga, "High-speed propulsion of flexible nanowire motors: Theory and experiments," *Soft Matter*, vol. 7, pp. 8169–8181, 2011.
- [32] E. Purcell, "The efficiency of propulsion by a rotating flagellum," *Proc. Nat. Acad. Sci. USA*, vol. 94, pp. 11307–11311, 1997.
- [33] S. Palagi, V. Pensabene, L. Beccai, B. Mazzolai, A. Menciassi, and P. Dario, "Design and development of a soft magnetically-propelled swimming microrobot," in *Proc. IEEE Int. Conf. Robot. Autom.*, Shanghai, China, 2011, pp. 5109–5114.
- [34] P. Garstecki, P. Tierno, D. Weibel, F. Sagues, and G. Whitesides, "Propulsion of flexible polymer structures in a rotating magnetic field," *J. Phys.-Condens. Mat.*, vol. 21, pp. 204110–204117, 2009.
- [35] J. Singleton, E. Diller, T. Andersen, S. Régnier, and M. Sitti, "Micro-scale propulsion using multiple flexible artificial flagella," in *Proc. IEEE/RSJ Int. Conf. Intell. Rob. Syst.*, San Francisco, CA, USA, 2011, pp. 1687–1692.
- [36] C. Wiggins and R. Goldstein, "Flexive and propulsive dynamics of elastica at low Reynolds number," *Phys. Rev. Lett.*, vol. 80, pp. 3879–3882, 1998.
- [37] T. Yu, E. Lauga, and A. Hosoi, "Experimental investigations of elastic tail propulsion at low Reynolds number," *Phys. Fluids*, vol. 18, pp. 091701-1–091701-4, 2006.
- [38] M. Manghi, X. Schlagberger, and R. Netz, "Propulsion with a rotating elastic nano-rod," *Phys. Rev. Lett.*, vol. 96, pp. 068101-1–068101-4, 2006.
- [39] N. Coq, O. du Roure, J. Marthelot, D. Bartolo, and M. Fermigier, "Rotational dynamics of a soft filament: Wrapping transition and propulsive forces," *Phys. Fluids*, vol. 20, pp. 051703-1–051703-4, 2008.
- [40] B. Qian, T. R. Powers, and K. S. Breuer, "Shape transition and propulsive force of an elastic rod rotating in a viscous fluid," *Phys. Rev. Lett.*, vol. 100, pp. 078101-1–078101-4, 2008.
- [41] S. Spagnolie and E. Lauga, "The optimal elastic flagellum," *Phys. Fluids*, vol. 22, pp. 031901-1–031901-15, 2010.
- [42] Z. Nagy, O. Ergeneman, J. J. Abbott, M. Hutter, A. Hirt, and B. J. Nelson, "Modeling assembled-mems microrobots for wireless magnetic control," in *Proc. IEEE Int. Conf. Robot. Autom.*, Pasadena, CA, USA, 2008, pp. 874–879.
- [43] B. J. Kirby, *Micro- and Nanoscale Fluid Mechanics: Transport in Microfluidic Devices*. Cambridge, U.K.: Cambridge Univ. Press, 2009.
- [44] B. Qian, H. Jiang, D. Gagnon, K. S. Breuer, and T. R. Powers, "Minimal model for synchronization induced by hydrodynamic interactions," *Phys. Rev. E*, vol. 80, pp. 061919-1–061919-10, 2009.
- [45] M. J. Kim, M. J. Kim, J. C. Bird, T. R. Powers, and K. S. Breuer, "Particle image velocimetry experiments on a macro-scale model for bacterial flagellar bundling," *Exp. Fluids*, vol. 37, pp. 782–788, 2004.
- [46] G. Hwang, R. Braive, A. Cavanna, A. Querghi, I. Robert-Philip, A. Beveratos, S. Haliyo, I. Sagnes, and S. Régnier, "Electro-osmotic propulsion of helical nanobelt swimmers," *Int. J. Rob. Res.*, vol. 30, no. 7, pp. 806–819, 2011.
- [47] S. M. Jeon, G. H. Jang, H. C. Choi, S. H. Park, and J. O. Park, "Magnetic navigation system for the precise helical and translational motions of a microrobot in human blood vessels," *J. Appl. Phys.*, vol. 111, pp. 07E702-1–07E702-3, 2012.
- [48] S. Tottori, L. Zhang, F. Qiu, K. Krawczyk, A. Franco-Obregon, and B. J. Nelson, "Magnetic helical micromachines: Fabrication, controlled swimming, and cargo transport," *Adv. Mater.*, vol. 24, pp. 811–816, 2012.
- [49] T. Ui, R. Hussey, and R. Roger, "Stokes drag on a cylinder in axial motion," *Phys. Fluids*, vol. 27, pp. 787–795, 1984.
- [50] V. Arabagi, B. Behkam, E. Cheung, and M. Sitti, "Modeling of stochastic motion of bacteria propelled spherical microbeads," *J. Appl. Phys.*, vol. 109, pp. 114702-1–114702-10, 2011.
- [51] J. Gray and G. Hancock, "The propulsion of sea-urchin spermatozoa," *J. Exp. Biol.*, vol. 322, pp. 802–814, 1955.
- [52] R. Butt, *Introduction to Numerical Analysis Using MATLAB*. Hingham, MA, USA: Infinity Sci., 2007.
- [53] E. Diller, Z. Ye, and M. Sitti, "Rotating magnetic micro-robots for versatile non-contact fluidic manipulation of micro-objects," in *Proc. IEEE/RSJ Int. Conf. Intell. Rob. Syst.*, San Francisco, CA, USA, 2011, pp. 1291–1296.
- [54] B. Gorgel, "Nanosprings take shape," *Science*, vol. 309, pp. 1683–1684, 2005.
- [55] M. Yasui, M. Ikeuchi, and K. Ikuta, "Magnetic micro actuator with neutral buoyancy and 3d fabrication of cell size magnetized structure," in *Proc. IEEE Int. Conf. Robot. Autom.*, St. Paul, MN, USA, 2012, pp. 745–750.
- [56] T. G. Leong, P. A. Lester, T. L. Koh, E. K. Call, and D. H. Gracias, "Surface tension-driven self-folding polyhedra," *Langmuir*, vol. 23, no. 17, pp. 8747–8751, 2007.



**Zhou Ye** (S'11) received the B.S. degree in mechanical engineering and automation from Tsinghua University, Beijing, China, in 2008 and the M.S. degree in mechanical engineering from Columbia University, New York, NY, USA, in 2010. He is currently working toward the Ph.D. degree in mechanical engineering with Carnegie Mellon University, Pittsburgh, PA, USA.

His current research interests include microscale manipulation, magnetic actuation, biomicrodevices, and microfluidic systems.



**Stéphane Régnier** received the Ph.D. degree in mechanics and robotics from the University of Pierre and Marie Curie, Paris, France, in 1996.

He is currently a Professor with the Institute of Intelligent Systems and Robotics (ISIR), University of Pierre and Marie Curie. He has been the Head of the ISIR micromanipulation team since 2001. His research interests include micro- and nanomanipulation, teleoperation and haptic feedback at the nanoscale, micromechanics, and biological cell characterization.



**Metin Sitti** (S'94–M'00–SM'08) received the B.Sc. and M.Sc. degrees in electrical and electronics engineering from Bogazici University, Istanbul, Turkey, in 1992 and 1994, respectively, and the Ph.D. degree in electrical engineering from the University of Tokyo, Tokyo, Japan, in 1999.

He was a Research Scientist with the University of California at Berkeley, Berkeley, CA, USA, during 1999–2002. He is currently a Professor with the Department of Mechanical Engineering and Robotics Institute, Carnegie Mellon University, Pittsburgh, PA, USA. He is the Director of the NanoRobotics Lab and Center for BioRobotics. His research interests include micro/nanorobotics, bioinspired and biohybrid miniature mobile robots, bioinspired micro/nanomaterials, and micro/nanomaterials.

Dr. Sitti received the SPIE Nanoengineering Pioneer Award in 2011, the National Science Foundation CAREER Award in 2005, and the IBM Smarter Planet Award in 2012. He received the Best Paper Award at the IEEE/RSJ International Conference on Intelligent Robots and Systems in 1998 and 2009, the Best Biomimetics Paper Award at the IEEE Robotics and Biomimetics Conference in 2004, and the Best Video Award at the IEEE Robotics and Automation Conference in 2002. He was appointed Adamson Career Faculty Fellow during 2007–2010. He was the Vice President for Technical Activities at the IEEE Nanotechnology Council during 2008–2010. He was elected Distinguished Lecturer of the IEEE Robotics and Automation Society for 2006–2008. He is the current active Editor-In-Chief of the *Journal of Micro-Bio Robotics*.